Optimal Measurement Policy for Linear Measurement Systems with Applications to UAV Network Topology Prediction

Abolfazl Razi, Senior Member, IEEE

Abstract—Dynamic network topology can pose important challenges to communication and control protocols in networks of autonomous vehicles. For instance, maintaining connectivity is a key challenge in unmanned aerial vehicle (UAV) networks. However, tracking and computational resources of the observer module might not be sufficient for constant monitoring of all surrounding nodes in large-scale networks. In this paper, we propose an optimal measurement policy for network topology monitoring under constrained resources. To this end, We formulate the localization of multiple objects in terms of linear networked systems and solve it using Kalman filtering with intermittent observation. The proposed policy includes two sequential steps. We first find optimal measurement attempt probabilities for each target using numerical optimization methods to assign the limited number of resources among targets. The optimal resource allocation follows a waterfall-like solution to assign more resources to targets with lower measurement success probability. This provides a 10% to 60% gain in prediction accuracy. The second step is finding optimal on-off patterns for measurement attempts for each target over time. We show that a regular measurement pattern that evenly distributed resources over time outperforms the two extreme cases of using all measurement resources either in the beginning or at the end of the measurement cycle. Our proof is based on characterizing the fixed-point solution of the error covariance matrix for regular patterns. Extensive simulation results confirm the optimality of the most alternating pattern with up to 10-fold prediction improvement for different scenarios. These two guidelines define a general policy for target tracking under constrained resources with applications to network topology prediction of autonomous systems.

Index Terms—Kalman filtering, target tracking, mobility prediction, linear measurement systems, UAV networks, topology control.

I. INTRODUCTION

Network topology plays an essential role in developing efficient communication, control, and task coordination algorithms for networks of autonomous nodes. For instance, consider a vehicular ad-hoc network (VANET) that relies on vehicle-to-vehicle (V2V) communication for traffic control. When driving in a sparsely populated remote urban area without roadside infrastructure, connectivity loss becomes an issue for vehicles with limited communication ranges [1]. Note

¹Copyright (c) 2015 IEEE. Personal use of this material is permitted. However, permission to use this material for any other purposes must be obtained from the IEEE by sending a request to pubs-permissions@ieee.org. The author is with the School of Informatic, Computing and Cyber Systems at Northern Arizona University.

This material is based upon the work supported by the National Science Foundation under Grant No. 1755984. This work is also partially supported by the Arizona Board of Regents (ABOR) under Grant No. 1003073.

that for example, the range of IEEE 802.11p used in the wireless access in vehicular environments (WAVE) platform designed to support intelligent transportation systems (ITS) is about 1 km [2]. This range for reliable communication through the LTE-V2V system is slightly higher but not more than a few kilometers [3]. For these scenarios, connectivity-aware networking protocols can significantly improve the reliability of information exchange [4].

The impact of dynamic topology on communication performance becomes even more critical in the emerging unmanned aerial vehicle (UAV) networks due to several reasons [5], [6]. Firstly, the autonomous drones can fly at higher speeds than ground vehicles making more dynamic network topologies. Secondly, the motion trajectories of UAVs are 3D and more probabilistic compared to the 2D trajectories of ground vehicles that are influenced by the man-made and natural patterns (e.g., roads and rivers). Thirdly, the tracking systems of UAVs are more constrained due to the limited payload size, power supply and computational capacity of UAVs. Therefore, developing optimal methods for predicting future locations of network nodes can be more challenging in flying ad-hoc networks (FANET). This problem has great practical importance due to the unprecedented recent growth in using UAV systems for different applications [7]–[11].

An accurate estimation of current network topology can significantly boost the performance of networking and control protocols in autonomous systems. For instance, communication between drones with limited communication ranges can undergo frequent link failures and loss of connectivity if the network topology is not properly incorporated into the routing protocol [12], [13]. To address this issue, several routing protocols with enhanced performance are recently proposed to accommodate the time-variant network topology [14]. However, most existing algorithms do not provide guaranteed QoS since they make decisions solely based on the current network status ignoring the predictability of future network topology. Recently, a few research projects are focused on developing predictive algorithms that incorporate the predicted network topology into decision-making strategies at different layers of communication protocols [15]-[17].

A. Review of Mobility Prediction

A key requirement to facilitate *predictive* networking is developing an efficient method to monitor and predict the network topology [18]. Network topology prediction can be realized by predicting the upcoming locations of network

nodes $\mathcal{N} = \{n_1, n_2, \dots, n_N\}$, as it enables developing the timevarying *contact graph* based on the nodes' communication ranges. For instance, if the communication range of nodes for a reliable communication is R and the location of node n_i at time t is represented by $l_i(t)$, then the *contact graph* would be $\mathcal{G}(t) = \{V, E(t)\}$, where $V = \mathcal{N}$ is the set of nodes and E(t) is the set of edges with elements $E_{ij}(t) = 1$ for $d(l_i(t), l_j(t)) \leq R$ and $E_{ij}(t) = 0$ otherwise.

Mobility prediction can be categorized into two mainstream trends of data-driven and model-based methods. In datadriven methods, frequent motion patterns are exploited by analyzing large datasets. This information can be used to implement more efficient terrestrial wireless networks to accommodate traffic mobility [19]. Similar data-driven methods are proposed to model the motion patterns of pedestrians [20], vehicles [21], and animals [22]. The second approach is using *model-based* methods to predict the future location of an object by processing the history of its motion trajectory. The drawback of model-based methods is their reliance on models customized for specific object types with different mobility models such as random walk [23], random waypoints [24], and Gaussian Morkov mobility model (GMMM) [25]. Consequently, they are not typically applicable to a network of heterogeneous nodes.

A more general framework for target tracking is using the linear measurement system framework, where the kinematic equations are presented in terms of state transition equations [26]. In this formulation, Kalman filtering is proven to be the optimal way of state estimation. Also, Kalman filtering with intermittent observation can be used to predict the future locations of the target by applying state update equations when the measurement is absent [27]. Therefore, it performs both estimation and prediction tasks. The only drawback of this method is that the motion dynamics of the target is not included in the prediction phase, which ignores the utility of the object-specific motion properties in the prediction process. Recently, a unified mobility prediction model is proposed based on Kalman filtering with intermittent observations, where the state-transition equations provide the flexibility of predicting node locations based on the history of motion trajectory, whereas a generative model for the probabilistic input captures the class-specific mobility patterns [18].

Several works have been proposed to evaluate the performance of Kalman filtering under different scenarios. However, the majority of these methods overlook the power of using optimized measurement policies in achieving higher prediction accuracy. Indeed, most performance analysis works take an unrealistic assumption of making measurements at all time slots (e.g., [28], [29]). Therefore these approaches do not apply to practical UAV networks with extremely constrained tracking resources and limited processing power. Some other works consider intermittent observation, but presume that the lack of observation is only due to measurement failures (e.g., [30]–[32]), and not based on developing an optimized measurement policy that is addressed in our paper.

Mobility prediction relies on locating network nodes using an arbitrary tracking technology such as ultrasound [33], video [34], acoustic [35], laser [36], radar and Lidar systems [37], [38], imagery [39], [40], infrared [41], and hybrid methods [17]. An important challenge that naturally arises in practical systems is the lack of sufficient tracking resources for constant monitoring of all surrounding nodes. For instance, the Reigel VZ-400 laser scanning system that is commonly used in tracking systems (e.g., [42]), provides an accuracy of 5 mm within 600 meters with the vertical scan speed of 3 to 120 lines per second and horizontal scan speed of 0° to 60° per second. Therefore, completing full 3D scanning can take a very long time and exhaust computational resources. Similar constraints apply to image-based [43], TDOA-based Radar [44], RSSbased [45], and hybrid localization methods [17]. Moreover, the measurement success rate depends on the objects' material, size, shape, speed, and distance from the observer that should be taken into account when assigning measurement resources. We show in this paper that developing optimized tracking attempt patterns for each target can significantly improve the overall performance of the localization system.

This paper aims at solving this problem for a scenario, where an observer (a network node or a separate identity) intends to monitor surrounding nodes using Kalman filtering with intermittent observation under conditions (e.g., maximum number of parallel targets, measurement time, measurement success rate, motion turbulence, and measurement noise) that are imposed by the utilized tracking system. This problem is solved in two sequential steps. We first find the optimal probability of measurement attempt for each target, denoted by α_i . Next, we find the optimal way of splitting $\alpha_i T$ measurement resources that are allocated for target n_i over consecutive T time slots. The core idea is to characterize the impact of measurement patterns on the evolution of estimation/prediction error for fault-tolerant tracking systems. The obtained policy is general and applicable to topology prediction of dynamic networks with mobile users of any type. The rest of this paper is organized as follows. Section II elaborates the details of the utilized mobility model. Section III offers an optimal measurement policy through two sequential steps. Simulation results are provided in section IV, followed by concluding remarks in section V.

II. MOBILITY MODEL

We suppose that an observer intends to predict the locations of N drones during T consecutive time slots, as depicted in Fig. 1. For instance, in a battlefield between two adversary UAV networks, a central tracking system can monitor all nodes of the adversary network and share that information with self network members. Likewise, in a network of autonomous drones, each drone may need to predict other nodes' upcoming locations to select a proper relay node. Before proceeding with the details of formulation, let us provide a summary of notations in Table I.

The motion of a flying object n_i can be modeled using Dubin's curve in terms of the second order differential equations. For instance, for a one-dimensional motion, we have

$$\begin{cases} x(t+dt) = x(t) + v(t)dt \\ v(t+dt) = v(t) + a(t)dt \end{cases}$$
 (1)

Table I: Summary of Notations.

| Parameter | Definition | | | | |
|------------------------------------|---|--|--|--|--|
| N | Number of targets (network nodes) | | | | |
| M | Number of tracking resources | | | | |
| T | Number of measurement time slots | | | | |
| A, B, C | State transition matrices | | | | |
| $\mathbf{s}_{i}(k)$ | State vector for target n_i at time k | | | | |
| $\mathbf{u}_i(k), \mathbf{y}_i(k)$ | Input and observation vectors | | | | |
| $\mathbf{w}_i(k), \mathbf{v}_i(k)$ | System and observation noise vectors | | | | |
| $\mathbf{Q}_i(k), \mathbf{R}_i(k)$ | System and observation noise covariance matrices | | | | |
| $\hat{\mathbf{P}}_{i}(k)$ | Error covariance matrix for target target n_i at time k | | | | |
| $\gamma_i[k]$ | Observation success indicator for target n_i at time k | | | | |
| λ_i | Observation success probability: $P(\gamma_i[k] = 1) = \lambda_i$ | | | | |
| β_{ik} | Observation attempt indicator for target n_i at time k | | | | |
| α_i | Observation attempt probability: $P(\beta_{ik} = 1) = \alpha_i$ | | | | |

Equivalently, in a discrete-time model, after converting $x(t) = x(kdt) \rightarrow x(k)$, we have

$$\begin{cases} x(k+1) = x(k) + v(k)dt \\ v(k+1) = v(k) + a(k)dt \end{cases}$$
 (2)

After extending these equations into 3D space, we obtain the following state transition equations:

$$\begin{cases} \mathbf{s}_{i}[k+1] &= A\mathbf{s}_{i}[k] + B\mathbf{u}_{i}[k] + \mathbf{w}_{i}[k], \\ \mathbf{y}_{i}[k] &= \gamma_{i}[k]C\mathbf{s}_{i}[k] + \mathbf{v}_{i}[k], \end{cases}$$
(3)

with

$$\mathbf{s}_{i}[k] = \begin{bmatrix} x_{i}[k] \ y_{i}[k] \ z_{i}[k] \ v_{xi}[k] \ v_{yi}[k] \ v_{zi}[k] \end{bmatrix}^{T}, \text{ (state vector)}$$

$$\mathbf{u}_{i}[k] = \begin{bmatrix} a_{xi}[k] \ a_{yi}[k] \ a_{zi}[k] \end{bmatrix}^{T}, \text{ (input vector)}$$

$$\mathbf{y}_{i}[k] = \begin{bmatrix} \mathbf{y}_{xi}[k] \ y_{yi}[k] \ y_{zi}[k] \end{bmatrix}^{T}, \text{ (observation vector)}$$

$$A_{6\times6} = \begin{bmatrix} \mathbf{I}_{3\times3} & dt\mathbf{I}_{3\times3} \\ \mathbf{0}_{3\times3} & \mathbf{I}_{3\times3} \end{bmatrix}, B_{6\times3} = \begin{bmatrix} \mathbf{0}_{3\times3} & dt\mathbf{I}_{3\times3} \end{bmatrix}^{T},$$

$$C_{3\times6} = \begin{bmatrix} \mathbf{I}_{3\times3} & \mathbf{0}_{3\times3} \end{bmatrix},$$

$$\mathbf{v}_{i}[k] \sim \mathcal{N}(\mathbf{0}_{3\times1}, \mathbf{R}_{i}), \mathbf{w}_{i}[k] \sim \mathcal{N}(\mathbf{0}_{6\times1}, \mathbf{Q}_{i}),$$
(4)

where, $\mathbf{s}_i[k]$ is the 6×1 state vector of node n_i at discrete time k that represents its location (x,y,z) and velocities (v_x,v_y,v_z) in 3D space, and $\mathbf{y}[k]$ is the 3×1 observation vector including the observation values of the tracking system. Here, $\mathbf{u}[k]$ is a 3×1 input vector that represents the accelerations (or equivalently the exerted forces) along the three coordinate axes, and can be used to capture the class-specific mobility features of an object [18]. Also, $\mathbf{w}_{6\times 1}$ and $\mathbf{v}_{3\times 1}$ are zero mean Gaussian random vectors with covariance matrices $\mathbf{Q}_{6\times 6}$ and $\mathbf{R}_{3\times 3}$ that represent the model turbulence and observations noise 2 .

The measurements success is modeled as a sequence of Bernoulli distributed random variables $(\gamma_i[k] \in \{0,1\}, \Pr(\gamma_i[k] = 1) = \lambda_i)$ [48]. It is known that an optimal estimation of the state vectors (in MMSE sense) can be obtained using Kalman filtering with the following steps

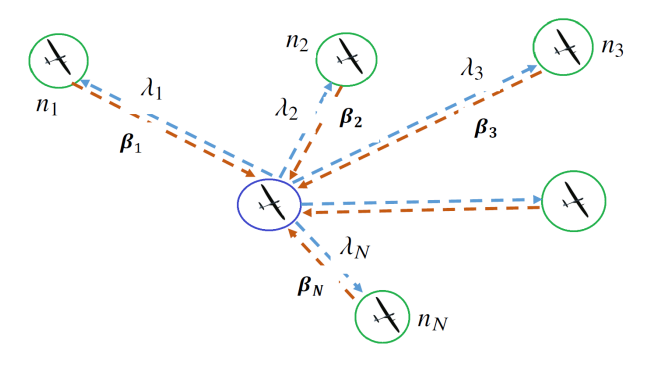


Figure 1: An observer UAV tracks the mobility of N surrounding drones, where β_i is a binary value representing the measurement attempt and $0 \le \lambda_i \le 1$ represents the probability of successful measurement completion.

(hereafter, we omit the subscript i representing the node index for notation convenience, unless it is necessary):

$$\begin{cases} \tilde{\mathbf{s}}[k] = A\hat{\mathbf{s}}[k-1] + B\mathbf{u}[k-1] \\ \tilde{P}[k] = A\hat{P}[k-1]A^T + Q \end{cases}$$
 (time update eqs),
$$\begin{cases} K[k] = \tilde{P}[k]C^T(C\tilde{P}[k]C^T + R)^{-1} \\ \hat{\mathbf{s}}[k] = \tilde{\mathbf{s}}[k] + K[k](y[k] - C\tilde{\mathbf{s}}[k]), \text{ (measurement eqs),} \\ \hat{P}[k] = (I - K[k]C)\tilde{P}[k] \end{cases}$$
 (5)

where the measurement update equations are performed only for $\gamma[k] = 1$ and we set $\hat{\mathbf{s}}[k] = \tilde{\mathbf{s}}[k], \hat{P}[k] = \tilde{P}[k]$ for $\gamma[k] = 0$ [48]. Under some mild convergence conditions on matrices A, B, C, and Q, namely the observability of (A, C), the controllability of (A, B), the stabilizability of $(A, Q^{1/2})$ and the bounded system and measurement noise covariances) the sequential error covariance matrices $\hat{P}[k]$ for any initial value converge to a unique limit, which is the solution of the following modified discrete-time algebraic *Riccati* equation (MARE) [27]:

$$M(P; \lambda, R, Q) = APA^{T} + Q - \lambda APC^{T} (CPC^{T} + R)^{-1} CPA^{T},$$

$$P = M(P; \lambda, R, Q).$$
(6)

The solution of (6) is not known in general, but it is known that the convergence of $\hat{P}[k]$ is ensured if the observation availability occurs with probability $\lambda \geq \lambda_c$, where λ_c is a critical value with known upper and lower bounds [49]. In most studies, the presumption of taking measurements at all time slots is used, where $\gamma[k]$ models the measurement failure. However, it is impractical to track all targets at all time slots in large-scale networks. In the next section, we formulate the problem of optimally assigning available measurement resources to monitor target nodes.

III. MEASUREMENT POLICY DESIGN

Suppose that an observer intends to predict the locations of N targets during T time slots. We consider a constrained measurement resource scenario, where a total of $M = \rho N$ measurement resources are available per time slot, where ρ (0 < ρ ≤ 1) is the ratio of the number of tracking resources

²Note that the state vector can equivalently be represented in *polar coordinate system* by conversion $r = \sqrt{x^2 + y^2}$, $\theta = tan^{-1}(y/x)$, $v_r = \hat{r}$, $\omega = \hat{\theta}$, and the rest of the equations follow [18], [46]. Alternative formulations for rotatory and fixed-wing drones are also possible [47].

to the number of targets. Note that if $\rho > 1$, then the following optimization is irrelevant and each observer can track all targets in parallel. We are addressing the case that the number of resources M is smaller than the number of targets N.

The goal is to optimally assign the available $L = \rho NT$ resources among N targets across T time slots, so that the overall prediction error in terms of the expected summation of the trace of covariance matrices (i.e. $\sum_{i=1}^{N} \sum_{t=1}^{T} \mathbb{E}[tr(P_i(t)])$ is minimized. We use expected value of the covariance matrix, since it is a random matrix for intermittent observation ($\rho \neq 1$) [49]. Let us define the measurement attempt strategy in terms of a binary matrix $\mathcal{B} = [\beta_{it}]_{N \times T}$, where $\beta_{it} = 1$ represents a measurement attempt for target i at time t. Therefore, the goal is to find an optimal matrix \mathcal{B}^* such that the overall prediction accuracy is maximized under the constraint $\sum_{i=1}^{N} \beta_{it} \leq \rho N$ for $t = 1, 2, \ldots, T$.

Note that the maximum number of traceable targets in parallel (M) is defined by the utilized tracking system. T is the number of measurement time-slots in each optimization interval. T should be selected large enough to let the Kalman filtering converge, which is > 100 for our scenario. On the other hand, T should be selected small enough to have relatively constant system conditions $(\mathbf{R}_i, \mathbf{Q}_i, \lambda_i)$ during one optimization interval noting the average speed of targets.

This problem can be broken down into two sequential subproblems. Firstly, we allocate the total measurement resources among N targets. To this end, we define attempt probabilities $\alpha_1, \alpha_2, \ldots, \alpha_N$ to make measurements of objects n_1, n_2, \ldots, n_N , under the constrained resources, i.e., $\sum_{i=1}^N \alpha_i < \rho N$. The impact of α_i is that we should replace the measurement success probability λ_i in (6) with the product of this probability with attempt probability $\alpha_i \lambda_i$. Therefore, the evolution of P_i depends on the choice of α_i (section III-A). The next step is to assign the $\alpha_i T$ allocated tracking resources for target n_i , over consecutive time slots so that $\sum_{t=1}^T \beta_{it} \leq \alpha_i T$ for $i=1,2,\ldots,T$ (section III-B).

A. Optimal Measurement Attempt Strategy

The vector $\alpha = (\alpha_1, \alpha_2, \dots, \alpha_N)$, is the vector of measurement attempt probabilities. In order to find the optimal measurement probabilities, we consider minimizing the expected value of the accumulated squared errors over consecutive T time slots as follows:

$$(\alpha_1^*, \alpha_2^*, \dots, \alpha_N^*) = \operatorname{argmin} \sum_{i=1}^N \sum_{k=1}^T \mathbb{E} \left[tr(\hat{P}_i[k]) \right]$$
subject to: $0 \le \alpha_i \le 1$, for $i = 1, 2, \dots, N$,
$$\alpha_i \lambda_i \ge \lambda_i^{(c)},$$

$$\alpha_1 + \alpha_2 + \dots + \alpha_N \le \rho N,$$
 (7)

where $\lambda_i^{(c)}$ is the critical value for measurement success probability to have a bounded expected error covariance. In this case, it has been shown that the covariance matrix converges to the solution of the modified discrete-time algebraic *Riccati* equation (MARE), defined in Eq. (6) [27]. However, this problem is not tractable because the covariance matrices follow a stochastic process, due to the probabilistic

measurement success rate, and also it depends on the initial value $\hat{P}_i[0]$. If the trace of error covariance matrix converges to a limit (under the stability conditions), we can solve the following equation:

$$(\alpha_1^*, \alpha_2^*, \dots, \alpha_N^*) = \operatorname{argmin} \sum_{i=1}^N \lim_{k \to \infty} E[tr(\hat{P}_i[k])]$$
subject to: $0 \le \alpha_i \le 1$, for $i = 1, 2, \dots, N$,
$$\alpha_i \lambda_i \ge \lambda_i^{(c)},$$

$$\alpha_1 + \alpha_2 + \dots + \alpha_N \le \rho,$$
 (8)

that approximates (7) for sufficiently large T.

This problem can be solved using numerical methods. The idea is to characterize $E[tr(\hat{P}_i[k])]$ based on α_i and then find the optimal α_i . The solution of this problem determines the measurement attempt probability for each target to have an optimal total prediction accuracy. However, it does not admit a closed-form solution. In [50], we proposed an online optimization algorithm based on particle swarm optimization (PSO) to solve this problem under dynamic situations. In this paper, we used three additional numerical optimization methods including genetic algorithm (GA), simulated annealing (SA), and gradient descent (GD) to show that the results are not sensitive to the choice of optimization method. The complexity of PSO scales linearly with the number of targets and hence is applicable to large-scale systems.

The constraint $\alpha_i \gamma_i \geq \gamma_i^{(c)}$ implies a *waterfall-like* solution for this problem, since the lower measurement success probability γ_i for an object is compensated by a higher attempt probability α_i to exceed the critical value of the successful measurement completion $\gamma_i^{(c)}$. For instance, in practical scenarios, objects in further distances with poorer measurement quality must be tracked more frequently.

B. Optimal Measurement Pattern Design

The second step is to develop actual measurement patterns to assign the $\alpha_i T$ measurement resources for target n_i over T time slots for optimized performance. We represent the measurement patterns by a binary matrix, \mathcal{B} . To draw guidelines of this method, we start with a single target scenario, which is equivalent to specifying a row of \mathcal{B} , denoted by $\boldsymbol{\beta}_T^i = (\beta_{i1}, \beta_{i2}, \ldots, \beta_{ik})$ for a bounded Hamming weight. Again, for simplicity, we drop the node index i and simply use $\boldsymbol{\beta}_T = (\beta_1, \beta_2, \ldots, \beta_T)$ for an arbitrary row of \mathcal{B} . We denote the desired performance metric (e.g., the trace of the estimation/prediction error covariance matrix) at time k with x_k . Obviously $\{x_k\}_{k=1}^T$ forms a stochastic time-series, where transition from x_k to x_{k+1} is governed by the success of taking measurement at time k as follows:

$$x_{k+1} = \begin{cases} f(x_k) & \text{if } \beta_k = 0 \text{ (measurement absent)} \\ g(x_k) & \text{if } \beta_k = 1 \text{ (measurement present)} \end{cases}$$
(9)

In order to find the asymptotic solution for this problem, we consider $T \to \infty$. First, we note that f(x) > g(x), since otherwise the measurements are irrelevant. The goal is to find an optimal sequence $\boldsymbol{\beta}_T = (\beta_1, \dots, \beta_T)$ under the constrain $\sum_{k=1}^T \beta_k \leq \alpha T$ such that $1/T \sum_{k=1}^T x_k$ is minimized. This

problem is computationally expensive and involves examining all possible patterns of β_T . A reasonable approximation is to consider the asymptotic solution for the steady-state conditions after x_k converges to a limit. Under these conditions we can use $1/T \sum_{k=1}^{T} x_k \approx x_T$ for $T \rightarrow \infty$. Hereafter, we take this approach and consider only regular patterns, since irregular patterns are irrelevant for $T \to \infty$. In this case, after some transitional periods, x_k approaches a value which is the solution of the corresponding fixed point equation. Here, we consider that $\alpha = 1/2$ and we plan to find an optimal order for the sequence of T/2 ones and T/2 zeros for β_T , such that the resulting steady-state error for the selected sequence is asymptotically optimal. As an illustrative example, consider the following three patterns:

the following three patterns:
$$\beta_T^{(a)} = [101010 \dots 10101010], \text{ most alternating pattern.}$$

$$\beta_T^{(b)} = [111 \dots 111 000 \dots 000], \text{ measurements at beginning,}$$

$$\beta_T^{(e)} = [000 \dots 000 111 \dots 111] \text{ measurements at the end}$$

$$\beta_T^{(e)} = [000 \dots 000 111 \dots 111] \text{ measurements at the end}$$

$$\beta_T^{(e)} = [001011 \dots] \text{ random pattern.}$$

$$\beta_T^{(e)} = [001011 \dots] \text{ random pattern.}$$

$$(10) \text{ Lemma III.1. The affinity and concavity of } f(x) \text{ and } h(x)$$

For the two extreme patterns $(\boldsymbol{\beta}_T^{(b)})$ and $\boldsymbol{\beta}_T^{(e)}$, we have two different sections for x_k , each of which approaches the solutions of two fixed point equations, namely x = f(x)and x = g(x), after some initial transitions. Under the most alternating pattern $\beta_T^{(a)}$, the odd and even terms $(x_{2k-1} \text{ and } x_{2k})$ converge to the fixed point solutions of $x = g \circ f(x) = h(x)$ and $x = f \circ g(x) = l(x)$, respectively. Lets denote the solutions of the fixed point equations by x_f , x_g , x_h and x_l as follows:

$$x_f = f(x_f),$$
 $x_g = g(x_g),$ $x_h = h(x_h),$ $x_l = l(x_l).$ (11)

These points for an exemplary functions for one dimensional state transition equations are depicted in Fig. 2. To show that the asymptotic error for the most alternating pattern (a pattern with most transitions between 0 and 1 for β_k and β_{k+1}) is lower than that of the first two extreme cases, we need to show the following inequality:

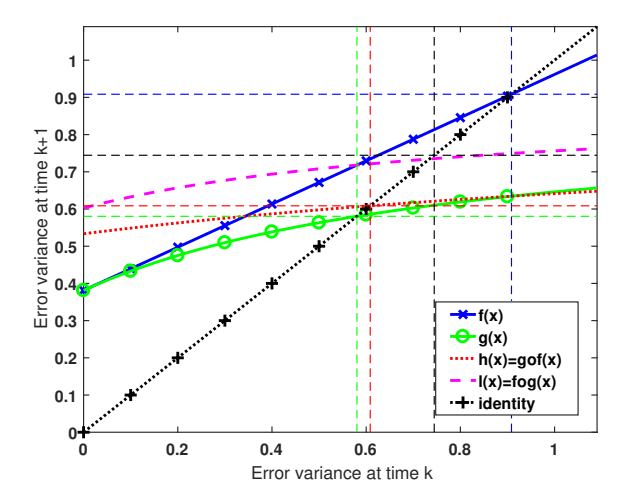
$$x_l + x_h < x_f + x_g. ag{12}$$

To this end, we prove this inequality for a wider range of functions with given conditions and then verify the conditions for our scenario.

Theorem III.1. Consider that x_f , x_g , x_h , x_l are the solutions of fixed point equations defined in (11). Then we have $x_l + x_h < \infty$ $x_f + x_g$, if the following conditions are held:

- 1) 0 < g(x) < f(x) for all x > 0
- 2) f(x) and g(x) are monotonic increasing and we have 0 < g'(x) < f'(x) < 1 for all x > 0
- 3) f(0) = g(0) > 0
- 4) f''(x) = 0 and g''(x) < 0 (affinity and concavity conditions)

We first state a set of lemmas that are direct implications of the conditions 1-4. Then, we provide the proof of theorem in Appendix.



Lemma III.1. The affinity and concavity of f(x) and h(x)along with their monotonic increasing property imply the concavity and monotonic increasing properties for h(x) = $g \circ f(x) = g(f(x))$ and $l(x) = f \circ g(x) = f(g(x))$.

Proof. We have [51]

$$x_1 > x_2 \rightarrow f(x_1) > f(x_2) \rightarrow g(f(x_1)) > g(f(x_2)) \rightarrow h(x_1) > h(x_2)$$

f is concave $\rightarrow f(\alpha x + \bar{\alpha} y) > \alpha f(x) + \bar{\alpha} f(y)$

$$\frac{g \text{ is monotonic increasing}}{g(g(\alpha x + \bar{\alpha}y))} g(f(\alpha x + \bar{\alpha}y)) > g(\alpha f(x) + \bar{\alpha}f(y))$$

$$\frac{g \text{ is concave}}{g(g(\alpha x + \bar{\alpha}y))} g(f(\alpha x + \bar{\alpha}y)) > \alpha g(f(x)) + \bar{\alpha}g(f(y))$$

$$\rightarrow h(\alpha x + \bar{\alpha}y) > \alpha h(x) + \bar{\alpha}h(y) \tag{13}$$

which holds for l(x) as well. Here, we have $\bar{\alpha} = 1 - \alpha$.

Lemma III.2. Conditions 2, 3 and 4 imply that f(x), g(x)have fixed point solutions for x = f(x) and g = g(x).

Proof. The proof is by contradiction. Lets assume that g(x)has no fixed point solution for x = g(x). This implies that g(x) > x for any x. In other words, the curve g(x) stays over the identity curve i(x) = x, and hence g(x) > x for all x, due to the continuity of g(x). Now set x > g(0)/(1 - g'(0)). We have:

$$g(x) < g(0) + xg'(0) = x(g(0)/x + g'(0))$$

$$= x(1 - g'(0) + g'(0)) = x,$$

$$\Longrightarrow g(x) < x,$$
(14)

that contradicts the assumption g(x) > x. Note that the inequality g(x) < g(0) + xg'(0) is due to the concavity of g(x). Therefore, there always exists a solution for f(x) = x. The same argument applies to f(x).

Lemma III.3. Assumptions 3 and 1 imply that l(0) > h(0).

Proof.
$$l(0) = f \circ g(0) = f \circ f(0) > g \circ f(0) = h(0)$$
.

Lemma III.4. The function $h(x) = g \circ f(x)$ has a fixed point solution $x_h = h(x_h)$ that satisfies $x_g < x_h < x_f$.

Proof. See Appendix.

Lemma III.5. The function $l(x) = f \circ g(x)$ has a fixed point solution $x_l = l(x_l)$ that satisfies $x_g < x_l < x_f$.

Proof. The proof is similar to Lemma III.4.

C. Guidelines to design optimal measurement patterns.

Suppose that conditions 1 to 4 of theorem III.1 hold for transformations $T_f: x \to f(x)$ for $\beta = 0$ and $T_g: x \to g(x)$ for $\beta = 1$. If $\beta_T = [\beta_1, ..., \beta_T]$ represent the measurement pattern for a target with tracking attempt probability $\alpha_i = 1/2$, we have $|\beta_T|_1 = T/2$. Then, theorem III.1 implies that the most alternating pattern $\beta_T^{(a)} = [0101010...]$ in (10), asymptotically outperforms the two extreme cases of taking all measurements in the beginning $\beta_T^{(b)}$ or at the end $\beta_T^{(e)}$, as verified by the simulation results in section IV. Through applying the above-mentioned approach to newly defined functions $f_2 = f \circ f$ and $g_2 = f \circ g$, it is straightforward to show that the symmetric pattern of taking two consecutive measurements and holding the following two time slot (according to pattern [001100110011]) outperforms the extreme case of taking all measurements in a row, but not as good as the most alternating method. We note that the stable points of f_2 and g_2 are equivalent to those of f and g, used for the extreme cases. With similar arguments and using the proof by induction, we can show that all other symmetric patterns of taking mconsecutive measurements and holding the following m timeslots outperform the extreme cases as well. Also, intensive numerical results in section IV show that the most alternating pattern (most transitions between "0"s and "1"s) determines the optimal measurement policy. The intuition behind this fact is that, it is more beneficial to take a measurement right after time slots without measurements to eliminate the prediction error whereas taking multiple measurements in a row is not much beneficial. Note that the gain of the most alternating pattern $\boldsymbol{\beta}_T^{(a)}$ over the most extreme patterns $\boldsymbol{\beta}_T^{(b)}$ and $\boldsymbol{\beta}_T^{(e)}$ is higher than the improvement gain with respect to random patterns $\beta_T^{(r)}$. Also, note that choosing the right pattern does not impose any additional computational complexity to the system, and can be adopted independent of the computationally intensive step proposed in section III-A.

A sample measurement pattern based on the above guidelines is presented in Fig. 3, for a scenario with N=5 target nodes and M=2 measurement resources per time slot, based on the optimal measurement probabilities $\alpha_1=1/2$, $\alpha_2=1/4$, $\alpha_3=1/8$, $\alpha_4=3/8$, $\alpha_5=3/4$. Developing measurement policies based on the above guideline for an arbitrary set of measurement probabilities can be realized with simple iterative algorithms (such as initialize, try patterns and re-permute).

D. Utility of the results in UAV location prediction

The following theorem proves that the prediction error variance of the Kalman filtering framework defined in (3) satisfies the conditions of theorem III.1. Therefore, the derived

guidelines for optimal measurement patterns in section III-C apply to tracking multiple flying objects under constrained resource measurements.

Theorem III.2. If x_k represent the estimation error variance of equations in (3) using Kalman filtering framework, and we define f(x) and g(x) in (9), then f(x) and g(x) satisfy conditions (1-4) of theorem III.1.

Proof. See Appendix.

IV. SIMULATION RESULTS

In this section, we present simulation results to assess the utility of the proposed measurement policy for accurate prediction of the locations of flying objects. The proposed policy is based on the optimality of measurement attempt probabilities in (8), and using the most alternating pattern discussed in section III-B.

A. Optimal Measurement Attempt Probability: Results

We first show that the solution of Kalman filtering with intermittent observation provided in (5) can be used to predict the position of an object based on processing the history of motion trajectory when the measurement result is absent.

Fig. 4 represents the localization of a single UAV hovering at a fixed altitude (a 2-D plane) under different measurement success rates (MSR). When the measurement success rate is close to 1, the main task of Kalman filtering is to estimate the current location based on the measurement results by eliminating the plant and observation noises. On the other hand, it provides an accurate prediction of the target location using state transition equations, in the absence of measurements. The prediction is more accurate for higher MSR values as expected.

Fig. 5, represents the results of PSO-based optimization applied to (8). Here, the goal is to obtain the optimal measurement attempt probabilities $(\alpha_1, \ldots, \alpha_N)$ for N=5 targets when there is only M=1 measurement resource available at each time slot. Each *particle* represents a measurement attempt probability vector $\alpha_1^{(p)}, \alpha_2^{(p)}, \ldots, \alpha_N^{(p)}$ for the given system conditions in terms of $\mathbf{Q}_i, \mathbf{R}_i), \lambda_i$. The algorithm randomly initializes the particles and iterates until all *particles* converge to the *best solution*, which provides the optimal measurement probabilities. The assessment of *particles* are based on the fix-point solution of the MARE equation in (6). We uses 100

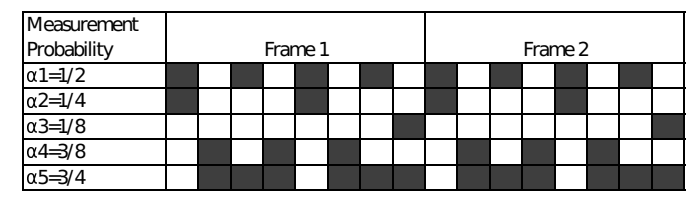


Figure 3: An exemplary pattern for N=5 targets and M=2 measurement resources for $\alpha_1=1/2,\ \alpha_2=1/4,\ \alpha_3=1/8,\ \alpha_4=3/8,\ \alpha_5=3/4.$ We have $\sum_{i=1}^5\alpha_i=M$ and no more than M=2 resources are used at each time slot $\sum_{i=1}^N\beta_{it}\leq M$, while we exhaust the reserved measurement resources for each target $\sum_{t=1}^T\beta_{it}=\alpha_iT$.

particles, and a maximum of 100 iterations for this simulation. Fig. 5(a) the measurement probabilities for three target drones, determined by the best particle in 100 iterations. It is seen that the algorithm converges after about 65 iterations. Fig. 5b presents the average error variances in MSE sense for randomly selected particles and the best particle. Apparently, the best particle outperforms the other particles. Mild variations of MSE after the convergence point in Fig. 5(b) is due to the probabilistic nature of the error covariance series that depends on the randomly generated initial error covariance and the randomly generated measurement pattern. Similar results are presented in Fig. 6 for 4 different scenarios. The waterfalllike property of the optimal measurement policy is clearly noticeable. The optimal solution assigns higher measurement attempt probabilities (α_i) for targets with lower measurement success probabilities (λ_i) .

One may suspect that the obtained optimal measurement attempt probabilities $(\alpha_i, \dots, \alpha_N)$ in (8) may be sensitive to the choice of numerical optimization method. In order to verify the accuracy of the results based on the PSO optimization, here we use three additional optimization methods including genetic algorithm (GA), simulated annealing (SA), and gradient descent (GD). We also include the equal attempt probability $(\lambda_1 = \lambda_2 = \lambda_3 = 1/3)$ that represents no optimization (NOP). The results for mobility equations with three different sets of success probabilities are shown in Table II. The rest of system parameters are N = 3, M = 1, dt = $0.01, \mathbf{Q}_{ii}^2 = 1, \mathbf{R}_{ii}^2 = 10$. The performance of each method is calculated by averaging the trace of error covariance matrix over R = 10 runs, N = 3 targets, and T = 1000 time slots (i.e. $\frac{1}{RNT}\sum_{r=1}^{R}\sum_{i=1}^{N}\sum_{t=1}^{T}tr(\hat{P}_{i}[t])$. The results show that most optimization methods perform almost equally (with a standard deviation between 1% to 4%) if the optimization parameters are selected properly. For instance, we used PSO with 80 particles and the maximum number of 100 iterations. Also, we used the initial temperature of 1 and the cooling factor of

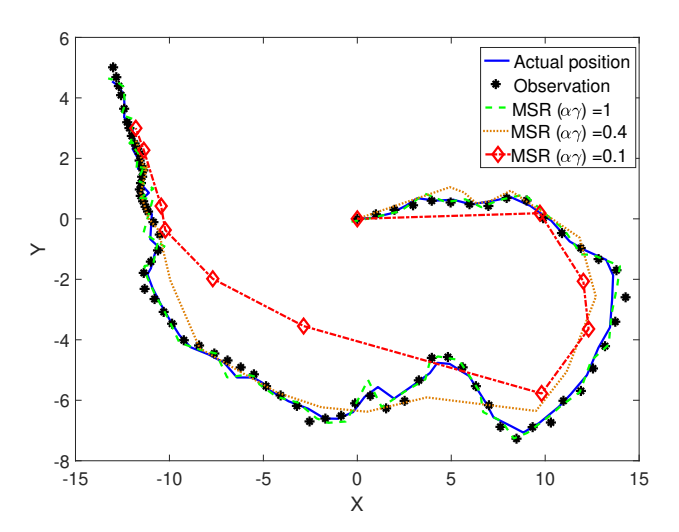
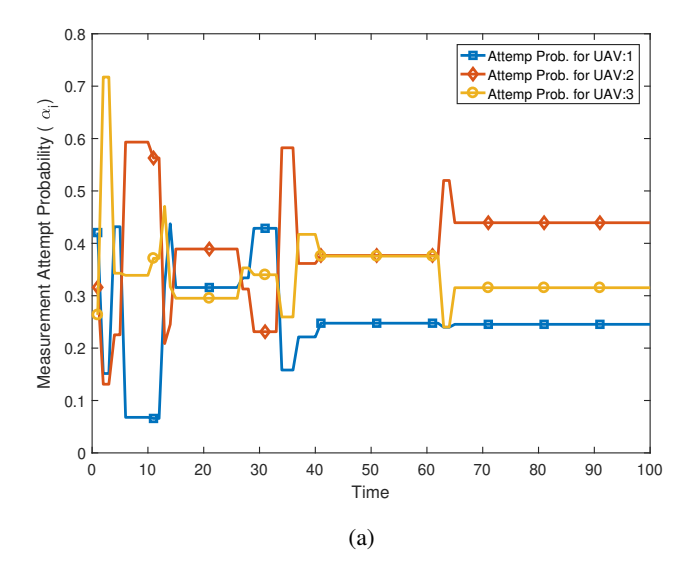


Figure 4: Kalman filtering is used to predict the location of a moving target in 2D plane when the measurement is absent. The measurement success rate (MSR) is denoted by $\alpha\gamma$.



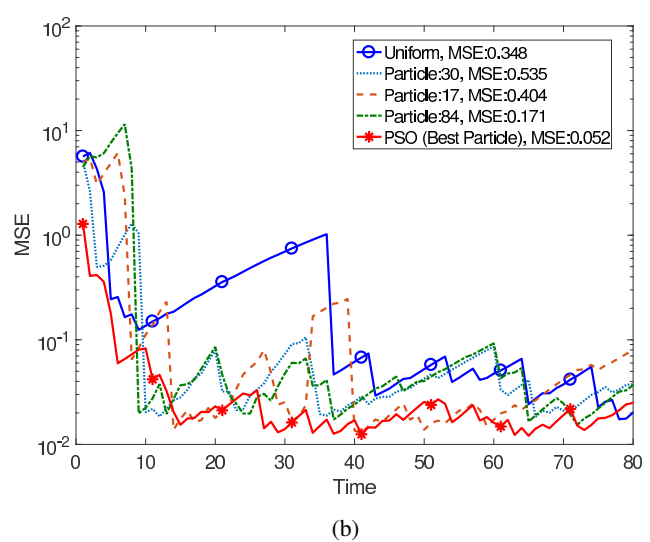


Figure 5: Finding optimal measurement attempt probabilities for N=5 targets using a PSO-based optimization framework with 100 particles. Each particle represents a randomly initialized probability vector $\alpha^{(p)} = (\alpha_1^{(p)}, \alpha_2^{(p)}, \dots, \alpha_5^{(p)})$; (a) the evolution of attempt probabilities for three UAVs; (b) the overall estimation accuracy in terms of mean squared errors (MSE) under different attempt probabilities.

0.8 for the SA method. For the GD method, we used the step value of $d\alpha = 0.01$ and averaged over 10 expectations to avoid trapping in local optima. For the GA, we used the MATLAB implementation with default parameters. The results confirm the benefit of the optimized resource allocation over no-optimization policy. For $\lambda_1 = \lambda_2 = \lambda_3 = 1/3$, all methods converge to $\alpha_1 = \alpha_2 = \alpha_3 = 1/3$, so no significant gain is achieved (Table II: top part). However, for the heterogeneous cases, the optimization methods consistently follow the aforementioned waterfall regime by assigning higher measurement attempt probabilities (α_i) for targets with lower measurement success probabilities (Λ_i) . For case 2 $(\lambda = (0.050.150.33)$, a gain of 10% to 15% is achieved using different optimization methods

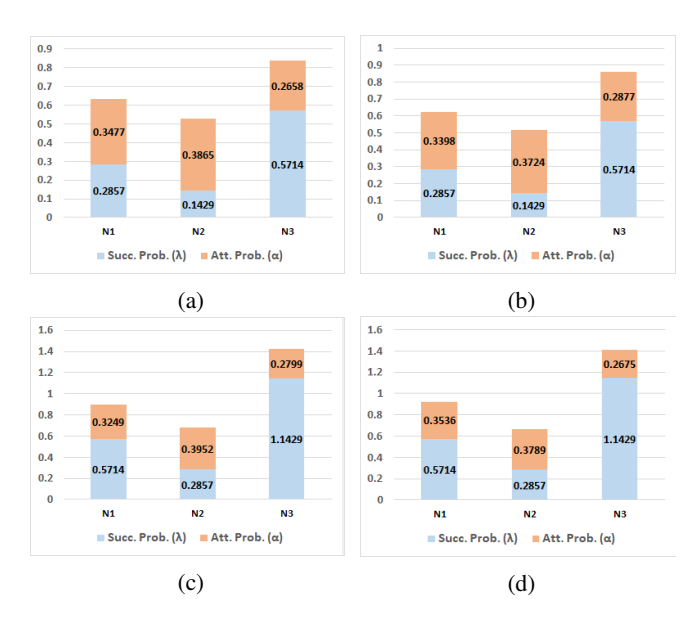


Figure 6: Waterfall-like property of the optimal measurement policy. Higher measurement attempt probabilities (α_i) are assigned to targets with lower measurement success probabilities (λ_i) . These results are for PSO with 80 particles and 100 iterations for different scenarios with (a): $\mathbf{R}_{ii} = 1, \sum_{i=1}^{3} \lambda_i = 1$, (b): $\mathbf{R}_{ii} = 10, \sum_{i=1}^{3} \lambda_i = 1$, (c): $\mathbf{R}_{ii} = 1, \sum_{i=1}^{3} \lambda_i = 2$, (d): $\mathbf{R}_{ii} = 10, \sum_{i=1}^{3} \lambda_i = 2$. The system noise power is $\mathbf{Q}_{ii} = 1$.

(Table II: middle part). This gain is 50% to 56% for case 3 ($\lambda = (0.050.150.33)/2$, highlighting that optimal measurement policy is more beneficial to keep the error covariance bounded when the measurement success probabilities are lower.

B. Optimal Measurement Attempt Pattern: Numerical Results

Figures 7 and 8 show that choosing the right measurement pattern can significantly improve the measurement accuracy. Fig. 7 compares the resulting error variance for a single target using different measurement patterns including the two extreme cases of taking all the measurements at the beginning $(\beta_T^{(b)})$ and at the end $(\beta_T^{(e)})$, as well as the most

Table II: Optimal Attempt Probability Using Different Optimization Methods.

| Method | Success Prob. | | | Attempt Prob. | | | MSE |
|---------|---------------|-------------|-------------|---------------|------------|------------|-------|
| Wiethou | λ_1 | λ_2 | λ_3 | α_1 | α_2 | α_3 | WISE |
| NOP | 0.33 | 0.33 | 0.33 | 0.333 | 0.333 | 0.333 | 263.6 |
| GD | 0.33 | 0.33 | 0.33 | 0.348 | 0.361 | 0.291 | 254.3 |
| GA | 0.33 | 0.33 | 0.33 | 0.325 | 0.330 | 0.319 | 261.8 |
| SA | 0.33 | 0.33 | 0.33 | 0.306 | 0.297 | 0.397 | 257.0 |
| PSO | 0.33 | 0.33 | 0.33 | 0.363 | 0.335 | 0.303 | 255.8 |
| NOP | 0.05 | 0.15 | 0.80 | 0.333 | 0.333 | 0.333 | 351.7 |
| GD | 0.05 | 0.15 | 0.80 | 0.494 | 0.321 | 0.185 | 295.7 |
| GA | 0.05 | 0.15 | 0.80 | 0.505 | 0.315 | 0.165 | 321.7 |
| SA | 0.05 | 0.15 | 0.80 | 0.476 | 0.326 | 0.198 | 302.1 |
| PSO | 0.05 | 0.15 | 0.80 | 0.383 | 0.400 | 0.217 | 305.1 |
| NOP | 0.025 | 0.075 | 0.40 | 0.333 | 0.333 | 0.333 | 849.1 |
| GD | 0.025 | 0.075 | 0.40 | 0.4090 | 0.4390 | 0.1510 | 385.1 |
| GA | 0.025 | 0.075 | 0.40 | 0.4870 | 0.3380 | 0.1480 | 426.0 |
| SA | 0.025 | 0.075 | 0.40 | 0.4390 | 0.4420 | 0.1180 | 410.6 |
| PSO | 0.025 | 0.075 | 0.40 | 0.3970 | 0.3970 | 0.2060 | 373.2 |

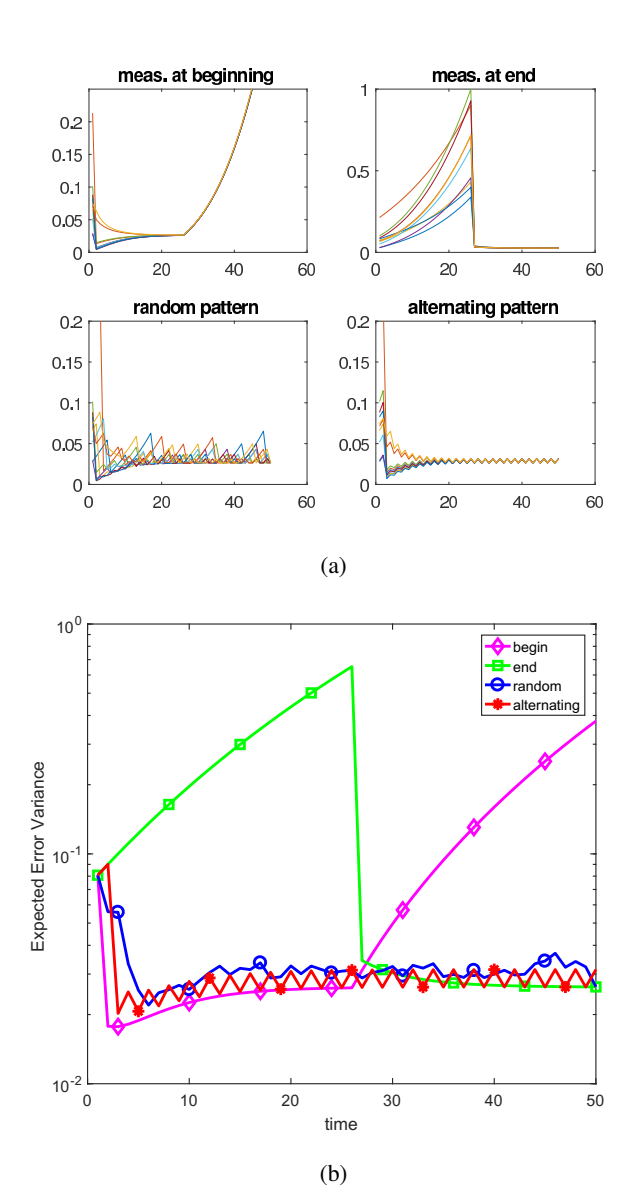


Figure 7: Comparison of the evolution of estimation error achieved by different measurement patterns including $\beta_T^{(b)}$, $\beta_T^{(e)}$, $\beta_T^{(a)}$, and $\beta_T^{(r)}$ defined in (10). The results correspond to a system with $\alpha = 1/2$ and $\gamma = 1$. (a): results for 10 scenarios with random initialization. (b): average over 10 scenarios.

alternating pattern $\beta_T^{(a)}$ and a random pattern $\beta_T^{(r)}$ in (10). The most alternating pattern significantly outperforms the extreme patterns in terms of the achieved average MSE, since the prediction accuracy of Kalman filtering dramatically drops in the absence of measurements (multiple consecutive zeros). It also slightly outperforms the random measurement pattern, where T/2 zeros and T/2 ones are randomly shuffled. Figure 8 summarizes the result for different measurement patterns and present the average prediction error versus the transition rate of the pattern. The transition rate of each pattern is calculated by counting the number of transitions from 0 to 1 and vice versa. The achieve localization accuracy in terms of the mean square error (MSE) can drop from 2.5 to 0.2 (a reduction by a factor of 10) if the most alternative pattern is selected.

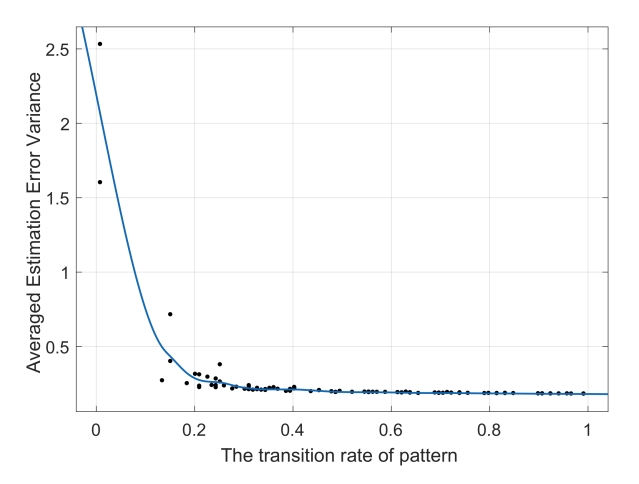


Figure 8: The average prediction error variance for different (and randomly selected) patterns including $\beta_T^{(a)}$, $\beta_T^{(e)}$ and $\beta_T^{(a)}$ defined in (10). Dot points are the error variance for a randomly initialized scenario ($P_i[0]$, \mathbf{Q}_i , \mathbf{R}_i) for different measurement patterns β_T , and the curve is the average of results over 100 scenarios with different initializations.

V. CONCLUSIONS

In this work, we considered the problem of network topology prediction using a general framework based on Kalman filtering with intermittent measurements for multiple targets under constrained tracking resources. The prediction error for each target follows a stochastic process that converges to a solution of a fixed-point equation determined by the modified discrete-time algebraic Riccati equation, provided that the successful measurement completion rate $\alpha_i \lambda_i$ exceeds a critical value, denoted by $\lambda_i^{(c)}$. We broke down this nonconvex problem into two subproblems. Firstly, we obtained the optimal measurement attempt probability for each target by minimizing the sum of the convergence limits of the corresponding MARE equations through a numerical PSObased optimization method. The solution exhibits a waterfalllike property by assigning higher attempt rates α_i for targets with poorer measurement conditions (lower $\lambda_i^{(c)}/\lambda_i$) such that the resulting measurement completion rate exceeds the target-specific critical value. Next, we proved that the $\alpha_i T$ reserved measurement resources for target n_i should be evenly distributed over T time-slots, since the pattern $[\beta_{i1}, \beta_{i2}, \dots \beta_{iT}]$ with a maximal transitions between measurement and silent time-slots yields a minimal convergence value for the error variance. These two guidelines can be used to develop optimized measurement patterns for real-world applications.

Although, we proposed this policy for network topology prediction of UAV networks to facilitate *predictive* communication and control algorithms, the proposed policy is general and applicable to other measurement systems operated based on Kalman filtering under constrained resources.

APPENDIX

Proof of lemma III.4: To prove the existence of x_h , we note that assumption 1 implies:

$$h(0) = g(f(0)) > 0 (15)$$

Also, the concavity of g() implies that for all $x > x_g$, we have:

$$x > x_g$$

$$\xrightarrow{(a)} g(x \frac{x_g}{x} + (1 - \frac{x_g}{x})0) > \frac{x_g}{x} g(x) + (1 - \frac{x_g}{x})g(0)$$

$$\xrightarrow{(b)} g(x_g) > \frac{x_g}{x} g(x)$$

$$\xrightarrow{(c)} x_g > \frac{x_g}{x} g(x)$$

$$\xrightarrow{(d)} g(x) < x,$$

$$(16)$$

where in (a), we used the concavitiy of g(), namely $g(\alpha x_1 + \bar{\alpha} x_2) > \alpha g(x_1) + \bar{\alpha} g(x_2)$ after setting $x_1 = x, x_2 = 0, \alpha = \frac{x_g}{x} > 0, \bar{\alpha} = 1 - \frac{x_g}{x} > 0$; (b) is due to the positivity of $\bar{\alpha}$ by assumption $x > x_g$ and the positivity of f(0) in assumption 3; (c) is due to x_g being the fixed point solution, namely $x_g = g(x_g)$; and (d) follows immediately. Following a similar argument, we can show that

$$f(x) < x, \text{ for } x > x_f. \tag{17}$$

Now, if we choose $x > \max(x_f, x_g)$, we have

$$g(f(x)) < f(x) < x$$
, for $x > \max(x_f, x_g)$. (18)

Continuity of h along with equations (15) and (18) implies that the fixed point equation x = h(x) has a unique solution x_h according to lemma III.2.

Now, we verify $x_h < x_f$ by contradiction. Suppose $x_h > x_f$, then we have the following set of rules:

$$x_{h} > x_{f}$$

$$\xrightarrow{(a)} h(x_{f}) > (1 - x_{f}/x_{h})h(0) + x_{f}/x_{h}h(x_{h})$$

$$\xrightarrow{(b)} h(x_{f}) > (1 - x_{f}/x_{h})h(0) + x_{f}$$

$$\xrightarrow{(c)} h(x_{f}) > x_{f}$$

$$\xrightarrow{(d)} h(x_{f}) > f(x_{f})$$

$$\xrightarrow{(e)} h(x_{f}) > g(x_{f})$$

$$\xrightarrow{(f)} f(x_{f}) > x_{f}$$

$$\xrightarrow{(g)} x_{f} > x_{f}, \qquad (19)$$

which is an obvious contradiction. We used the concavity of h() in (a), namely $h(\alpha x_1 + \bar{\alpha} x_2) > \alpha h(x_1) + \bar{\alpha} h(x_2)$ by setting $x_1 = 0, y = x_h, \alpha = 1 - x_f/x_h$; (b) is due to x_h being the fixed point solution, namely $h(x_h) = x_h$; (c) is due to the positivity of f(0) in condition 3 which implies h(0) = g(f(0)) > 0; (d) is due to x_f being the fixed point solution; (e) is due to f(x) > g(x) in condition 1; (f) is due to monotonicity of increasing function g(); and finally (g) is due to x_f being the fixed point solution.

Likewise, we can show that $x_h > x_g$ by contradiction. Suppose $x_h < x_g$, we have the following sequence of equations:

$$x_{h} < x_{g}$$

$$\xrightarrow{(a)} h\left(x_{g} \frac{x_{h}}{x_{g}} + (1 - \frac{x_{h}}{x_{g}})0\right) > \frac{x_{h}}{x_{g}} h(x_{g}) + (1 - \frac{x_{h}}{x_{g}})h(0)$$

$$\xrightarrow{(b)} h(x_{h}) > \frac{x_{h}}{x_{g}} h(x_{g})$$

$$\xrightarrow{(c)} x_{h} > \frac{x_{h}}{x_{g}} h(x_{g})$$

$$\xrightarrow{(d)} x_{g} > h(x_{g})$$

$$\xrightarrow{(e)} g(x_{g}) > h(x_{g})$$

$$\xrightarrow{(f)} x_{g} > f(x_{g})$$

$$\xrightarrow{(g)} g(x_{g}) > f(x_{g}),$$

$$\xrightarrow{(g)} g(x_{g}) > f(x_{g}),$$

$$(20)$$

which is in contradiction with f(x) > g(x) in condition 1. In (20), we used the concavity of h() in (a) by setting $x_1 = x_g, x_2 = 0, \alpha = x_h/x_g$; (b) is due the positivity of f(0) in 3; (d) is due to to x_h being the fixed point solution, namely $h(x_h) = x_h$; (d) is due to the positivity of x_g ; (e) is due to x_g being the fixed point solution; (f) is due to monotonicity of increasing function g(); and finally (g) is due to x_g being the fixed point solution. Therefore, x_h exists and we have $x_g < x_h < x_f$.

Proof of theorem III.1. In order to prove $x_h + x_l < x_f + x_g$, we note that the concavity of $h(x) = g \circ f(x)$ implies:

$$x_h = h(x_h) < h(x_f) + (x_h - x_f)h'(x_f)$$

$$\xrightarrow{(a)} x_h < g(x_f) + (x_h - x_f)f'(x_f)g'(x_f)$$

$$\xrightarrow{(b)} x_h < \frac{g(x_f) - x_f f'(x_f)g'(x_f)}{1 - f'(x_f)g'(x_f)},$$
(21)

where in (a) we used the chain rule of derivatives h'(x) = f'(x)g'(f(x)) and the identity $h(x_f) = g(f(x_f)) = g(x_f)$, and (b) follows immediately. In a similar way, we have

$$x_{l} = l(x_{l}) < l(x_{g}) + (x_{l} - x_{g})l'(x_{g})$$

$$\xrightarrow{(a)} x_{l} < f(x_{g}) + (x_{l} - x_{g})f'(x_{g})g'(x_{g})$$

$$\xrightarrow{(b)} x_{l} < \frac{f(x_{g}) - x_{g}f'(x_{g})g'(x_{g})}{1 - f'(x_{g})g'(x_{g})}.$$
(22)

Combining (21) and (22) yields:

$$x_h + x_l < \frac{g(x_f) - x_f f'(x_f) g'(x_f)}{1 - f'(x_f) g'(x_f)} + \frac{f(x_x) - x_g f'(x_g) g'(x_g)}{1 - f'(x_g) g'(x_g)}$$

$$= \frac{g(x_f) - x_f + x_f - x_f f'(x_f) g'(x_f)}{1 - f'(x_f) g'(x_f)}$$

$$+ \frac{f(x_g) - x_g + x_g - x_g f'(x_g) g'(x_g)}{1 - f'(x_g) g'(x_g)}$$

$$= \frac{g(x_f) - x_f}{1 - f'(x_f) g'(x_f)} + x_f + \frac{f(x_g) - x_g}{1 - f'(x_g) g'(x_g)} + x_g.$$
(23)

In order to prove $x_h + x_l < x_f + x_g$ (12), considering (23) it is sufficient to show that

$$\frac{g(x_f) - x_f}{1 - f'(x_f)g'(x_f)} + \frac{f(x_g) - x_g}{1 - f'(x_g)g'(x_g)} < 0, \tag{24}$$

which can be re-written as

$$\frac{f(x_g) - x_g}{x_f - g(x_f)} < \frac{1 - f'(x_g)g'(x_g)}{1 - f'(x_f)g'(x_f)}$$
(25)

Now, we use the assumption of f(x) being an affine function such that $f(x) = cx + x_0 \Rightarrow x_f = x_0/(1-c)$. consequently, the left hand side of the inequality in (25) is bounded as follows:

$$LHS = \frac{f(x_g) - x_g}{x_f - g(x_f)} = \frac{f(x_g) - x_g}{x_f - x_g} \frac{x_f - x_g}{x_f - g(x_f)}$$

$$\stackrel{(a)}{=} (1 - c) \frac{x_f - x_g}{x_f - g(x_f)}$$

$$\stackrel{(b)}{<} (1 - c) \frac{x_f - x_g}{x_f - (g(x_g) + (x_f - x_g)g'(x_g))}$$

$$\stackrel{(c)}{=} \frac{1 - c}{1 - g'(x_g)}, \tag{26}$$

where we used $f(x_g) = cx_g + x_0$ and $x_f = x_0/(1-c)$ in (a), the concavity of g(x) in (b) and $g(x_g) = x_g$ in (c). Similarly, we have

$$RHS = \frac{1 - f'(x_g)g'(x_g)}{1 - f'(x_f)g'(x_f)} = \frac{1 - cg'(x_g)}{1 - cg'(x_f)}$$

$$\stackrel{(a)}{>} 1 - cg'(x_g)$$

$$\stackrel{(b)}{>} 1 - cg'(x_g) - c + g'(x_g)$$

$$= (1 - c)(1 + g'(x_g))$$

$$\stackrel{(c)}{=} \frac{1 - c}{1 - g'(x_g)},$$
(27)

where we used $0 < g'(x_g)c < 1$ in (a), $g'(x_g) < f'(x_g) = c$ in (b) and the identity $\frac{1}{1-x} \approx 1 + x$ for small x in (c). Combining (27) and (26) yields the results in (25), that completes the proof.

Proof of theorem III.2 For the scalar case (one dimensional motions), we have:

$$x_{k+1} = \begin{cases} f(x_k) = A^2 x_k + Q, & \gamma_k = 0, \\ g(x_k) = A^2 x_k + Q - (A^2 C^2 x_k^2) / (C^2 x_k + R), & \gamma_k = 1. \end{cases}$$
(28)

Apparently, f(x) is a monotonically increasing affine function and we have f(0) = g(0) > 0, since the system error variance is a positive value (Q > 0). Also, the positivity of the measurement noise variance (R > 0) implies that f(x) > g(x) > 0 for x > 0. Now, we need to show that g(x) is a monotonically increasing concave function of x as follows:

$$g(x) = A^{2}x + Q - \frac{A^{2}C^{2}x^{2}}{C^{2}x + R} = Q + \frac{A^{2}Rx}{C^{2}x + R}$$

$$\Rightarrow g'(x) = \frac{A^{2}R^{2}}{(C^{2}x + R)^{2}}$$

$$\Rightarrow g''(x) = \frac{-A^{2}R^{2}C^{2}}{(C^{2}x + R)^{3}},$$
(29)

which implies that $0 < g'(x) < f'(x) = A^2$ and g''(x) < 0. Therefore, conditions (1-4) hold for the scalar case.

For the general case of multi-dimensional scenario, consider the following relations, based on the concept of functors.

$$tr(X_k) \quad \begin{matrix} X_k & \xrightarrow{F(X),G(X)} & X_{k+1} \\ \downarrow & & \downarrow & tr(X_{k+1}) \\ x_k & \xrightarrow{f(x),g(x)} & x_{k+1} \end{matrix}$$

where we have

$$\begin{cases} F(X_k) = AX_k A^T + Q, & (\beta_k = 0), \\ G(X_k) = AX_k A^T + Q - AX_k C^T (CX_k C^T + R)^{-1} CX_k A^T & (else), \end{cases}$$
(30)

and f() and g() represent the evolution of error variance (the trace of error covariance matrix) under transitions F() and G(). We use the concept of functors only to translate the transitions between covariance matrices (in Kalman filtering) into the transitions between desired estimation errors in terms of the trace of covariance matrices.

Conditions (1-3) are immediate results of the error covariance matrices being positive definite. To verify condition (4), consider that $X_k = x_k \tilde{X}$, where x_k is an arbitrarily distributed random variable to represent the trace of matrix X_k and \tilde{X} is a random PSD matrix with an arbitrary distribution and $\operatorname{tr}(\tilde{X}) = 1$, and independent of x_k . We have

$$X_{k+1} = AX_k A^T + Q = x_k A \tilde{X} A^T + Q$$

$$\Rightarrow x_{k+1} = f(x_k) = \operatorname{tr}(X_{k+1}) = \operatorname{tr}(x_k A \tilde{X} A^T + Q)$$

$$= x_k \underbrace{\operatorname{tr}(A^T A \tilde{X})}_{K_1} + \underbrace{\operatorname{tr}(Q)}_{K_2} = K_1 x_k + K_2. \tag{31}$$

Therefore, $f(x) = K_1x + K_2$ is obviously a monotonic increasing affine function. We proceed with inspecting g(x) as follows:

$$\begin{split} X_{k+1} &= x_k A \tilde{X} A^T + Q - x_k^2 A \tilde{X} C^T (x_k C \tilde{X} C^T + R)^{-1} C \tilde{X} A^T \\ \operatorname{tr}(X_{k+1}) &= x_k \operatorname{tr}(A^T A \tilde{X}) + \operatorname{tr}(Q) \\ &- x_k^2 \operatorname{tr}(A \tilde{X} C^T (x_k C \tilde{X} C^T + R)^{-1} C \tilde{X} A^T) \\ &= x_k \operatorname{tr}(A^T A \tilde{X}) + \operatorname{tr}(Q) \\ &- x_k^2 \operatorname{tr}(A \tilde{X} C^T R^{-1} (x_k C \tilde{X} C^T R^{-1} + I)^{-1} C \tilde{X} A^T) \\ &\stackrel{(a)}{=} x_k \operatorname{tr}(A^T A \tilde{X}) + \operatorname{tr}(Q) \\ &- x_k^2 \operatorname{tr}(A \tilde{X} C^T R^{-1} \Big(\sum_{n=0}^{\infty} (-x_k C \tilde{X} C^T R^{-1})^n \Big) C \tilde{X} A^T) \\ &= x_k \operatorname{tr}(A^T A \tilde{X}) + \operatorname{tr}(Q) \\ &- x_k^2 \operatorname{tr} \Big(\sum_{n=0}^{\infty} A \tilde{X} C^T R^{-1} (-x_k C \tilde{X} C^T R^{-1})^n C \tilde{X} A^T \Big) \\ &= x_k \operatorname{tr}(A^T A \tilde{X}) + \operatorname{tr}(Q) \\ &- \sum_{n=0}^{\infty} (-x_k)^{n+2} \operatorname{tr} \Big(C \tilde{X} A^T A \tilde{X} C^T R^{-1} (C \tilde{X} C^T R^{-1})^n \Big), \end{split}$$

where we used the Neumann series $(A + B)^{-1} = \sum_{n=0}^{\infty} A^{-1} (-BA^{-1})^n$ for $|B|_2 \le |A|_2$ in (a). Under stability

conditions required for the convergence of the Neumann series, we have $tr(x_k C\tilde{X}C^T) = tr(CXC^T) < tr(R)$ that implies $\alpha = tr(CXC^TR^{-1}) < 1$. Now note that

$$(x_k)^{n+2} \operatorname{tr} \left(C \tilde{X} A^T A \tilde{X} C^T R^{-1} (C \tilde{X} C^T R^{-1})^n \right)$$

$$= \operatorname{tr} \left(C X A^T A X C^T R^{-1} (C X C^T R^{-1})^n \right)$$

$$\leq \operatorname{tr} \left(C X X C^T R^{-1} (C X C^T R^{-1})^n \right)$$

$$\leq \operatorname{tr}(X) \operatorname{tr} \left((C X C^T R^{-1})^{n+1} \right)$$

$$\leq \operatorname{tr}(X) \alpha^{n+1}$$

$$\leq \operatorname{tr}(X) \alpha^n. \tag{33}$$

Therefore, the power series in (32) decay with n and the dominant term is $-x_k^2$, and hence $x_{k+1} = g(x_k)$ is convex in x_k , which verifies the conditions of theorem III.1 for the proposed measurement mechanism.

REFERENCES

- [1] A. M. Abdelgader and W. Lenan, "The physical layer of the IEEE 802.11p WAVE communication standard: the specifications and challenges," in *Proceedings of the world congress on engineering and computer science*, vol. 2, 2014, pp. 22–24.
- [2] Y. Yao, L. Rao, and X. Liu, "Performance and reliability analysis of IEEE 802.11 p safety communication in a highway environment," *IEEE transactions on vehicular technology*, vol. 62, no. 9, pp. 4198–4212, 2013.
- [3] S. Chen, J. Hu, Y. Shi, Y. Peng, J. Fang, R. Zhao, and L. Zhao, "Vehicle-to-everything (v2x) services supported by LTE-based systems and 5G," *IEEE Communications Standards Magazine*, vol. 1, no. 2, pp. 70–76, 2017.
- [4] G. Cecchini, A. Bazzi, B. M. Masini, and A. Zanella, "Performance comparison between IEEE 802.11 p and LTE-V2V in-coverage and out-of-coverage for cooperative awareness," in 2017 IEEE Vehicular Networking Conference (VNC). IEEE, 2017, pp. 109–114.
- [5] L. Gupta, R. Jain, and G. Vaszkun, "Survey of important issues in UAV communication networks," *IEEE Communications Surveys & Tutorials*, vol. 18, no. 2, pp. 1123–1152, Secondquarter 2016.
- [6] E. Yanmaz, M. Quaritsch, S. Yahyanejad, B. Rinner, H. Hellwagner, and C. Bettstetter, *Communication and Coordination for Drone Networks*. Cham: Springer International Ptive ublishing, 2017, pp. 79–91.
- [7] K. P. Valavanis and G. J. Vachtsevanos, "Uav applications: Introduction," Handbook of Unmanned Aerial Vehicles, pp. 2639–2641, 2015.
- [8] N. Zhao, X. Pang, Z. Li, Y. Chen, F. Li, Z. Ding, and M.-S. Alouini, "Joint trajectory and precoding optimization for uav-assisted noma networks," *IEEE Transactions on Communications*, vol. 67, no. 5, pp. 3723–3735, 2019.
- [9] N. Zhao, W. Lu, M. Sheng, Y. Chen, J. Tang, F. R. Yu, and K.-K. Wong, "Uav-assisted emergency networks in disasters," *IEEE Wireless Communications*, vol. 26, no. 1, pp. 45–51, 2019.
- [10] N. Mohamed, J. Al-Jaroodi, I. Jawhar, A. Idries, and F. Mohammed, "Unmanned aerial vehicles applications in future smart cities," *Technological Forecasting and Social Change*, 2018.
- [11] T. Adao, J. Hruska, L. Padua, J. Bessa, E. Peres, R. Morais, and J. Sousa, "Hyperspectral imaging: A review on uav-based sensors, data processing and applications for agriculture and forestry," *Remote Sensing*, vol. 9, no. 11, p. 1110, 2017.
- [12] G. Secinti, P. B. Darian, B. Canberk, and K. R. Chowdhury, "Sdns in the sky: Robust end-to-end connectivity for aerial vehicular networks," *IEEE Communications Magazine*, vol. 56, no. 1, pp. 16–21, 2018.
- [13] S. Rosati, K. Krużelecki, G. Heitz, D. Floreano, and B. Rimoldi, "Dynamic routing for flying ad hoc networks," *IEEE Transactions on Vehicular Technology*, vol. 65, no. 3, pp. 1690–1700, 2016.
- [14] T. Wang, Y. Cao, Y. Zhou, and P. Li, "A survey on geographic routing protocols in delay/disruption tolerant networks," *International Journal* of Distributed Sensor Networks, vol. 12, no. 2, p. 3174670, 2016.
- [15] S. Rosati, K. Kruzelecki, L. Traynard, and B. Rimoldi, "Speed-aware routing for uav ad-hoc networks," in *Globecom Workshops (GC Wkshps)*, 2013 IEEE. IEEE, 2013, pp. 1367–1373.

- [16] A. Rovira-Sugranes and A. Razi, "Predictive routing for dynamic uav networks," in Wireless for Space and Extreme Environments (WiSEE), 2017 IEEE International Conference on. IEEE, 2017, pp. 43–47.
- [17] A. Razi, C. Wang, F. Almaraghi, Q. Huang, Y. Zhang, H. Lu, and A. Rovira-Sugranes, "Predictive routing for wireless networks: Roboticsbased test and evaluation platform," in *Computing and Communication Workshop and Conference (CCWC)*, 2018 IEEE 8th Annual. IEEE, 2018, pp. 993–999.
- [18] H. Peng, A. Razi, F. Afghah, and J. Ashdown, "A unified framework for joint mobility prediction and object profiling of drones in uav networks," *Journal of Communications and Networks*, vol. 20, no. 5, pp. 434–442, 2018.
- [19] "Vehicular mobility trace of the city of cologne, germany," 2016. [Online]. Available: http://kolntrace.project.citi-lab.fr/
- [20] M. Bennewitz, W. Burgard, G. Cielniak, and S. Thrun, "Learning motion patterns of people for compliant robot motion," *The International Journal of Robotics Research*, vol. 24, no. 1, pp. 31–48, 2005.
- [21] S. Atev, O. Masoud, and N. Papanikolopoulos, "Learning traffic patterns at intersections by spectral clustering of motion trajectories," in *Intelli*gent Robots and Systems, 2006 IEEE/RSJ International Conference on. IEEE, 2006, pp. 4851–4856.
- [22] J.-G. Lee, J. Han, and X. Li, "A unifying framework of mining trajectory patterns of various temporal tightness," *IEEE Transactions* on Knowledge and Data Engineering, vol. 27, no. 6, pp. 1478–1490, 2015.
- [23] K. Lee, S. Hong, S. J. Kim, I. Rhee, and S. Chong, "Slaw: A new mobility model for human walks," in *INFOCOM 2009*, *IEEE*. IEEE, 2009, pp. 855–863.
- [24] Z. X. Ming, Z. Yue, Y. Fan, and A. Vasilakos, "Interference-based topology control algorithm for delay-constrained mobile ad hoc networks, in mobile computing," *IEEE Trans*, vol. 14, no. 4, pp. 742–754, 2015.
- [25] T.-E. Lu, K.-T. Feng et al., "Predictive mobility and location-aware routing protocol in mobile ad hoc networks," in GLOBECOM'05: IEEE Global Telecommunications Conference, Vols 1-6: DISCOVERY PAST AND FUTURE, 2005, pp. 899–903.
- [26] Y. Chan, A. Hu, and J. Plant, "A kalman filter based tracking scheme with input estimation," *IEEE transactions on Aerospace and Electronic Systems*, no. 2, pp. 237–244, 1979.
- [27] B. Sinopoli, L. Schenato, M. Franceschetti, K. Poolla, M. I. Jordan, and S. S. Sastry, "Kalman filtering with intermittent observations," in *Decision and Control*, 2003. Proceedings. 42nd IEEE Conference on, vol. 1, Dec 2003, pp. 701–708 Vol.1.
- [28] J. Guo, H. Zhang, Y. Sun, and R. Bie, "Square-root unscented kalman filtering-based localization and tracking in the internet of things," *Personal and ubiquitous computing*, vol. 18, no. 4, pp. 987–996, 2014.
- [29] J. Shi, Y. Li, G. Qi, and A. Sheng, "Extended target tracking filter with intermittent observations," *IET Signal Processing*, vol. 10, no. 6, pp. 592–602, 2016.
- [30] M. Nourian, A. S. Leong, S. Dey, and D. E. Quevedo, "An optimal transmission strategy for kalman filtering over packet dropping links with imperfect acknowledgements," *IEEE Transactions on Control of Network Systems*, vol. 1, no. 3, pp. 259–271, 2014.
- [31] W. Li, Y. Jia, and J. Du, "Distributed kalman consensus filter with intermittent observations," *Journal of the Franklin Institute*, vol. 352, no. 9, pp. 3764–3781, 2015.
- [32] X. Liu, L. Li, Z. Li, T. Fernando, and H. H. Iu, "Stochastic stability condition for the extended kalman filter with intermittent observations," *IEEE Transactions on Circuits and Systems II: Express Briefs*, vol. 64, no. 3, pp. 334–338, 2016.
- [33] H. Chen, D. Ni, J. Qin, S. Li, X. Yang, T. Wang, and P. A. Heng, "Standard plane localization in fetal ultrasound via domain transferred deep neural networks," *IEEE journal of biomedical and health informatics*, vol. 19, no. 5, pp. 1627–1636, 2015.
- [34] M. Mueller, N. Smith, and B. Ghanem, "A benchmark and simulator for UAV tracking," in *European conference on computer vision*. Springer, 2016, pp. 445–461.
- [35] F. Ashkooti and R. Rashidy, "A distributed particle filter for acustic target tracking in wireless sensor networks," in 2016 IEEE 10th International Conference on Application of Information and Communication Technologies (AICT), Oct 2016, pp. 1–6.
- [36] Q. Liao, W. Zhang, P. Shi, and M. Liu, "A flexible object tracking system for planary motion," in *Real-time Computing and Robotics (RCAR)*, *IEEE International Conference on*. IEEE, 2016, pp. 362–367.
- [37] I. Cherepinsky, J. C. Derenick, J. M. Leland, C. Stathis, and B. A. Blakeslee, "Lidar-based vehicle distance measurement system," Oct. 23 2018, uS Patent App. 10/109,208.

- [38] R. Opromolla, G. Fasano, G. Rufino, M. Grassi, and A. Savvaris, "Lidar-inertial integration for uav localization and mapping in complex environments," in 2016 International Conference on Unmanned Aircraft Systems (ICUAS). IEEE, 2016, pp. 649–656.
- [39] D. Barman and U. M. Sharma, "A study on human activity recognition from video," in 2016 3rd International Conference on Computing for Sustainable Global Development (INDIACom), March 2016, pp. 2832– 2835.
- [40] W. Zhang, Z. Cui, D. Zhang, and H. Wang, "Design of a dual camera children monitoring system based on motion tracking technology," in 2017 IEEE International Instrumentation and Measurement Technology Conference (I2MTC), May 2017, pp. 1–5.
- [41] M. Rashid and M. A. Sebt, "Tracking a maneuvering target in the presence of clutter by multiple detection radar and infrared sensor," in 2017 Iranian Conference on Electrical Engineering (ICEE), May 2017, pp. 1917–1922.
- [42] J. Szulwic, P. Burdziakowski, A. Janowski, M. Przyborski, P. Tysikac, A. Wojtowicz, A. Kholodkov, K. Matysik, and M. Matysik, "Maritime laser scanning as the source for spatial data," *Polish Maritime Research*, vol. 22, no. 4, pp. 9–14, 2015.
- [43] Y. Xu, L. Pan, C. Du, J. Li, N. Jing, and J. Wu, "Vision-based uavs aerial image localization: A survey," in *Proceedings of the 2nd ACM SIGSPATIAL International Workshop on AI for Geographic Knowledge Discovery*. ACM, 2018, pp. 9–18.
- [44] S. Lee, W. Lee, and K. You, "Tdoa based uav localization using dualekf algorithm," in *International Conference on Control and Automation*. Springer, 2009, pp. 47–54.
- [45] O. Herekoglu, M. Hasanzade, E. Saldiran, A. Cetin, I. Ozgur, A. G. Kucukoglu, M. B. Ustun, B. Yuksek, R. Yeniceri, E. Koyuncu et al., "Flight testing of a multiple uav rf emission and vision based target localization method," in AIAA Scitech 2019 Forum, 2019, p. 1570.
- [46] D. Grymin and A. Crassidis, "Simplified model development and trajectory determination for a uav using the dubins set," in AIAA Atmospheric Flight Mechanics Conference, 2009, p. 6050.
- [47] M. Owen, R. W. Beard, and T. W. McLain, "Implementing dubins airplane paths on fixed-wing uavs," in *Handbook of Unmanned Aerial Vehicles*. Springer, 2015, pp. 1677–1701.
- [48] B. Sinopoli, L. Schenato, M. Franceschetti, K. Poolla, M. I. Jordan, and S. S. Sastry, "Kalman filtering with intermittent observations," *IEEE transactions on Automatic Control*, vol. 49, no. 9, pp. 1453–1464, 2004.
- [49] X. Shen, D. Rus, and M. H. Ang, "Bounds for kalman filtering with intermittent observations," in *Control Conference (ECC)*, 2015 European, July 2015, pp. 2842–2846.
 [50] A. Razi and F. Afghah, "Optimal measurement policy for predicting
- [50] A. Razi and F. Afghah, "Optimal measurement policy for predicting uav network topology," in Asilomar Conference on Signals, Systems and Computers, Oct 2017.
- [51] S. Boyd and L. Vandenberghe, Convex Optimization. Cambridge University Press, March 2004. [Online]. Available: http://www.amazon.com/exec/obidos/redirect?tag=citeulike-20&path=ASIN/0521833787



Abolfazl Razi is an assistant professor of Electrical Engineering at Northern Arizona University (NAU). He received his B.S., M.S. and PhD degrees, all in Electrical Engineering, respectively from Sharif University (1994–1998), Tehran Polytechnic (1999–2001), and University of Maine (2009–2013). Prior to joining NAU, he held two postdoctoral positions in the field of machine learning and predictive modeling at Duke University (2013–2014), and Case Western Reserve University (2014–2015). He is the recipient of several competitive awards including

the Best Research of MCI in 2008, Best Graduate Research Assistant of the Year Award from the College of Engineering, University of Maine in 2011, and the Best Paper Award from the IEEE/CANEUS Fly By Wireless Workshop in 2011. His current research interests include AI-enabled wireless networking, nonlinear compressive sensing, topology control, UAV networks, and predictive modeling.